

Article

Analysis of the Scaling Effects in the Area-Averaged Fraction of Vegetation Cover Retrieved Using an NDVI-Isoline-Based Linear Mixture Model

Kenta Obata ^{1,2,†}, Tomoaki Miura ² and Hiroki Yoshioka ^{1,*}

¹ Department of Information Science and Technology, Aichi Prefectural University, 1522-3 Ibara, Nagakute, Aichi 480-1198, Japan; E-Mail: yoshioka@ist.aichi-pu.ac.jp

² Department of Natural Resources and Environmental Management, University of Hawaii at Manoa, 1910 East West Road, Sherman 101, Honolulu, HI 96822, USA; E-Mail: tomoakim@hawaii.edu

[†] Current Affiliation: Department of Natural Resources and Environmental Management, University of Hawaii at Manoa, 1910 East West Road, Sherman 101, Honolulu, HI 96822, USA

* Author to whom correspondence should be addressed; E-Mail: yoshioka@ist.aichi-pu.ac.jp.

Received: 16 May 2012; in revised form: 11 July 2012 / Accepted: 11 July 2012 /

Published: 18 July 2012

Abstract: The spectral unmixing of a linear mixture model (LMM) with Normalized Difference Vegetation Index (NDVI) constraints was performed to estimate the fraction of vegetation cover (FVC) over the earth's surface in an effort to facilitate long-term surface vegetation monitoring using a set of environmental satellites. Although the integrated use of multiple sensors improves the spatial and temporal quality of the data sets, area-averaged FVC values obtained using an LMM-based algorithm suffer from systematic biases caused by differences in the spatial resolutions of the sensors, known as scaling effects. The objective of this study is to investigate the scaling effects in area-averaged FVC values using analytical approaches by focusing on the monotonic behavior of the scaling effects as a function of the spatial resolution. The analysis was conducted based on a resolution transformation model introduced recently by the authors in the accompanying paper (Obata *et al.*, 2012). The maximum value of the scaling effects present in FVC values was derived analytically and validated numerically. A series of derivations identified the error bounds (inherent uncertainties) of the averaged FVC values caused by the scaling effect. The results indicate a fundamental difference between the NDVI and the retrieved FVC from NDVI, which should be noted for accuracy improvement of long-term observation datasets.

Keywords: fraction of vegetation cover; scaling effect; monotonicity; NDVI; resolution transformation model

1. Introduction

Time series analysis of biophysical and climatological parameters is indispensable for studies of the Earth's climate, land, and hydrology systems and the interactions among these systems. Such analysis often relies on the information retrieved from reflectance spectra measured by satellite instruments [1,2]. The fraction of vegetation cover (FVC) is one method used to measure the horizontal spread of vegetation and is defined as the ratio of the vegetated area to the entire pixel area in a satellite image [3]. The FVC can be estimated from a reflectance spectrum via empirical or physical model-based techniques, such as the vegetation index (VI) model [4], spectral mixture analysis (linear mixture model, LMM) [3,5,6], and radiative transfer models [7]. Several types of FVC datasets have been produced using historical and current optical sensor data (Table 1). For example, the European Commission provided a dataset called fCover that was derived from an ensemble of satellites. The program used to compile this dataset is known as the Carbon Cycle and Change in Land Observation Products (CYCLOPS) with SPOT-VEGETATION [8]. The technique used in this work is based on neural networks and uses simulated data from radiative transfer models [9,10] to train the neural network. NOAA initiated a program called the Global Vegetation Processing System (GVPS), which has produced a data product known as the global vegetation fraction (GVF). The dataset covers over 30 years of observation term and used the Normalized Difference Vegetation Index (NDVI) [11] to estimate the FVC. Several other programs have been initiated more recently, including the compilation of the dataset called fCover from ENVISAT-MERIS, which uses a neural network with a radiative transfer model with eleven spectral bands [12]; the FVC products determined using Variable Multiple Endmember Spectral Mixture Analysis (VESMA) of data from a geostational satellite; MSG-SEVIRI [13], and the Vegetation Continuous Field (VCF) from MODIS [14] based on a regression tree algorithm.

Table 1. Summary of the major FVC-equivalent products.

	CYCLOPS	TOAVEG	LSA SAF	GVPS	GLCF
Source :	CNES, <i>etc</i>	ESA	EUMETSAT	NOAA	UMD
Product :	fCover [8]	fCover [12]	FVC [13]	GVF [11]	VCF [14]
Sensor :	VEGETATION	MERIS	SEVIRI	AVHRR	MODIS
Period :	1998–	2002–	2005–	1981–	2000–2001
Resolution :	1 km	300 m	3 km	1.1 km	500 m
Scale :	Global	Global	Europe and Africa	Global	Global

Long-term observations of biophysical quantities spanning several decades generally require integrated use of an ensemble of satellite sensors [15]. Such efforts have been widely applied in numerous studies involving land remote sensing applications [16–21]. Discrepancies between the characteristics of the data sets, such as the spectral band configuration or the spatial resolution, however,

introduce systematic biases into the parameter retrievals. These discrepancies can decrease the accuracy of the land observations as well as the predictions based on the datasets; thus, the effects of such discrepancies must be investigated thoroughly to identify mechanisms for rectifying the discrepancies. This study contributes to an improved understanding of the effects of spatial resolution discrepancies on the calculated area-averaged FVC values [22].

Conceptual approaches and measurement models related to the scale issues have been introduced by Strahler *et al.* [23] and Woodstock and Strahler [24] in the context of remote sensing. Comprehensive and intensive reviews on the scale issues and related problems have been provided by several researchers [23,25–30]. Although various types of problems have been investigated by numerous studies, monotonic behavior has not been fully analyzed. This work shed light on the monotonic aspects of the FVC retrieval algorithm within a framework of the modifiable area unit problem [31] originated from the field of spatial analysis, which was later introduced to the remote sensing community [25,26,28,29].

Scaling effects have been investigated extensively in the context of biophysical parameter retrievals, such as calculations of the vegetation index [32–35] leaf area index (LAI) [36–38] and FVC [22]. Several studies have attempted to derive an analytical expression for the differences between the area-averaged NDVI values at two extreme resolutions [33,35,39], the coarsest and finest resolution, called the lumped and distributed cases [34]. These investigations reported that an NDVI value can never reach its maximum or minimum values at an intermediate resolution between the two extreme cases. Our previous studies [40,41] showed that the area-averaged values of the NDVI reach maximum and minimum values at the two extreme resolutions under certain conditions. A proof was provided based on the monotonic behavior of the scaling effects. One question arose in the case of FVC calculations: Do the area-averaged FVC values change monotonically with the spatial resolution, similar to the case of the NDVI? The present study attempts to answer this question.

Spectral unmixing under NDVI constraints (the NDVI-isoline-based LMM) has been used to estimate FVC values. The technique has the advantages of both the VI and LMM approaches [35,42,43]. The retrieved FVC values may be degraded by scaling effects [22] because the NDVI (used in the algorithm) suffers from such effects. The sources of the scaling effects in the FVC and their monotonic behavior were previously investigated analytically [44]. Although that study analyzed several fundamental properties of the FVC scaling effects, a geometrical interpretation of the monotonic behavior and a thorough investigation of the key parameters that significantly influenced the error bounds were not performed. The present study investigates the FVC changes as a function of the spatial resolution, which corresponds to the number of pixels within a fixed area, as an extension of our previous study [41]. The analysis of the FVC scaling effects is based on the resolution transform model proposed in our previous work [41] that is about the scaling effects in the NDVI. In that work we have shown that the NDVI varies monotonically as a function of spatial resolution in a certain resolution sequence. As an extension of the work, we focus on the scale issues in the FVC that uses NDVI in the retrieval algorithm. Although the FVC retrieval algorithm discussed in this study uses NDVI as a parameter, there is no guarantee that the FVC varies monotonically as the NDVI does. This study addresses this issue.

The structure of this work is as follows. After the brief explanation of theoretical background, we clarify the monotonicity of scaling effects in FVC (Section 3). We then explain a geometric

relationship between the monotonic trend and endmember spectra by numerical experiments using simulated endmember spectra in Section 4, followed by a validation exercise in Section 5. Derivation of the maximum error bounds of the scaling effects and numerical simulation will be explained in Section 6. The discussion and conclusion sections (Sections 7 and 8, respectively) follow.

2. Background

2.1. NDVI-Isoline-Based LMM

A reflectance spectrum from a target pixel may be represented as a linear sum of the spectra corresponding to a set of representative surface types (endmember spectra) in a LMM. We assume here that a target field consists of vegetation and non-vegetation classes. Red and near-infrared (NIR) bands are considered. Under these assumptions, a modeled spectrum, $\hat{\rho} = (\hat{\rho}_r, \hat{\rho}_n)$ (where the subscripts r and n indicate red and NIR spectra, respectively), may be written as

$$\hat{\rho} = \hat{\omega}\hat{\rho}_v + (1 - \hat{\omega})\hat{\rho}_s, \quad (1)$$

where $\hat{\rho}_v = (\hat{\rho}_{v,r}, \hat{\rho}_{v,n})$ and $\hat{\rho}_s = (\hat{\rho}_{s,r}, \hat{\rho}_{s,n})$ are vegetation and non-vegetation endmember spectra in the model (the subscripts v and s indicate the vegetation and soil components, that is, non-vegetation land areas, respectively). The weight of a vegetation endmember, $\hat{\omega}$, represents the FVC in the LMM. A unity constraint is imposed in Equation (1). To retrieve the FVC, in general, $\hat{\omega}$ may be determined by minimizing a distance measure (e.g., the Euclidean norm) between the modeled spectrum and the measured spectrum [3]. The condition that determines the FVC then permits the vegetation index to be substituted for the reflectance spectrum. The choice of NDVI for defining the condition is known as the NDVI-isoline-based LMM [42,45]. The estimated value of the FVC may be expressed analytically by solving for $\hat{\omega}$ after equating a modeled and a target NDVI

$$\hat{\omega} = \frac{v - \hat{v}_s}{(1 - \hat{\eta})(v - \hat{v}_v) + \hat{v}_v - \hat{v}_s}, \quad (2)$$

where v is the NDVI from the target spectrum ($\rho = (\rho_r, \rho_n)$). The variables \hat{v}_v and \hat{v}_s are the NDVI from the vegetation and non-vegetation endmember spectra in the model, respectively. The variable $\hat{\eta}$ is the ratio of the L-1 norm of the vegetation endmember to the non-vegetation endmember.

$$v = \frac{\rho_n - \rho_r}{\rho_n + \rho_r}, \quad (3a)$$

$$\hat{v}_v = \frac{\hat{\rho}_{v,n} - \hat{\rho}_{v,r}}{\hat{\rho}_{v,n} + \hat{\rho}_{v,r}}, \quad (3b)$$

$$\hat{v}_s = \frac{\hat{\rho}_{s,n} - \hat{\rho}_{s,r}}{\hat{\rho}_{s,n} + \hat{\rho}_{s,r}}, \quad (3c)$$

$$\hat{\eta} = \frac{\hat{\rho}_{v,n} + \hat{\rho}_{v,r}}{\hat{\rho}_{s,n} + \hat{\rho}_{s,r}}. \quad (3d)$$

Under the two-endmember assumption, if an endmember spectra assumed in a model rigorously corresponds to the true endmember spectra over a target field, the spatially averaged FVC will be independent of the spatial resolution (the averaged FVC values must be true values) [44]; however,

accurately estimating the endmember spectra based on satellite data is difficult due to the surface heterogeneity or the existence of multiple endmember spectra within a pixel [45–48]. Therefore, the FVC values calculated using this algorithm are biased by the differences between the modeled and true endmember spectra. In this case, the FVC retrieval algorithm becomes a nonlinear function of the input spectra, and this nonlinearity is a source of scaling effects.

The analytical form of the biased FVC under the two-endmember assumption (the target field is modeled under the same assumption) can be derived according to the following steps. First, we assume that a measured spectrum, ρ , can be expressed as a combination of true endmember spectra ($\rho_v = (\rho_{v,r}, \rho_{v,n})$ and $\rho_s = (\rho_{s,r}, \rho_{s,n})$) with a true FVC value ω given by

$$\rho = \omega\rho_v + (1 - \omega)\rho_s. \quad (4)$$

We then rewrite the FVC estimate given in Equation (2) using Equation (4) as the target spectrum,

$$\hat{\omega} = \frac{\omega \cdot \det(\Delta\rho, \hat{\rho}_s) + \det(\rho_s, \hat{\rho}_s)}{\omega \cdot \det(\Delta\hat{\rho}, \Delta\rho_s) + \det(\Delta\hat{\rho}, \rho_s)}, \quad (5)$$

where

$$\Delta\rho = \rho_v - \rho_s, \quad (6a)$$

$$\Delta\hat{\rho} = \hat{\rho}_v - \hat{\rho}_s. \quad (6b)$$

2.2. Scaling Effects of the FVC on the Landsat7-ETM+

Scaling effects in the calculation of an area-averaged FVC can be seen in the data from Landsat7-ETM+. In order to clearly show the scaling effects, we conducted the following experiment using the data acquired on 7 July 2001 (Path:109, Row:36), which covers both urban and suburban regions in the Aichi prefecture in Japan. The spectral data of the size of 64×64 pixels (extracted from the original scene) was used in this experiment (Figure 1(a)). The spectral data was aggregated using an average-based moving block window into a data set comprising images at multiple resolutions ($2^i \times 2^i$ ($i = 0, 1, \dots, 5$)), as shown in Figure 2. The vegetation endmember spectra assumed in the algorithm was (0.05, 0.35). The effects of the endmember spectra on the scaling effects were demonstrated by assuming either of two non-vegetation spectra, (0.12, 0.14) and (0.18, 0.22), denoted as the “soil endmem.-1” and “soil endmem.-2”, respectively. The reflectance spectra of the target area and endmember spectra assumed in the model are plotted in Figure 1(b). The vegetation spectrum is denoted by the green circle, whereas the soil endmem.-1 and -2 spectra are denoted by the dark and light brown circles, respectively.

The averaged FVC values ($\bar{\omega}_j$) were computed as a function of the spatial resolution, which corresponds to the number of pixels within a fixed area (j). The scaling effects in the averaged FVC, calculated as the relative differences between the $\bar{\omega}_j$ and $\bar{\omega}_1$, were computed according to

$$\delta\omega = \frac{\bar{\omega}_j - \bar{\omega}_1}{\bar{\omega}_1}. \quad (7)$$

The relative differences obtained from the pair of spectra comprising the vegetation and soil endmem.-1 are indicated by the filled circles in Figure 3. The averaged FVC values as a function of the spatial

resolution, for the soil endmem.-2, are indicated by the filled squares (Figure 3). Using the pair of vegetation and soil endmem.-1 spectra, the averaged FVC increased as a function of the number of pixels (coarser to finer). By contrast, the averaged FVC decreased when the spectral pair comprising the vegetation and soil endmem.-2 spectra was assumed in the algorithm. The results clearly indicate that the magnitude and trends (increasing or decreasing) of the scaling effects depend heavily on the endmember spectra assumed in the model. The scaling effects also depend on the endmember spectra reflected from the target area. The mechanism underlying the scaling effects observed in the calculated FVC has not been previously elucidated. The present study aims to address this very issue.

Figure 1. (a) A false-color image of a target field used to simulate the scaling effects in an area-averaged FVC calculation; (b) the reflectance spectra of the field and endmember spectra assumed in the model. One vegetation endmember spectrum assumed in the algorithm was (0.05, 0.35), denoted by a green circle. Two non-vegetation spectra were assumed: (0.12, 0.14) and (0.18, 0.22), that is, “soil endmem.-1” and “soil endmem.-2”, indicated by the dark and light brown circles, respectively.

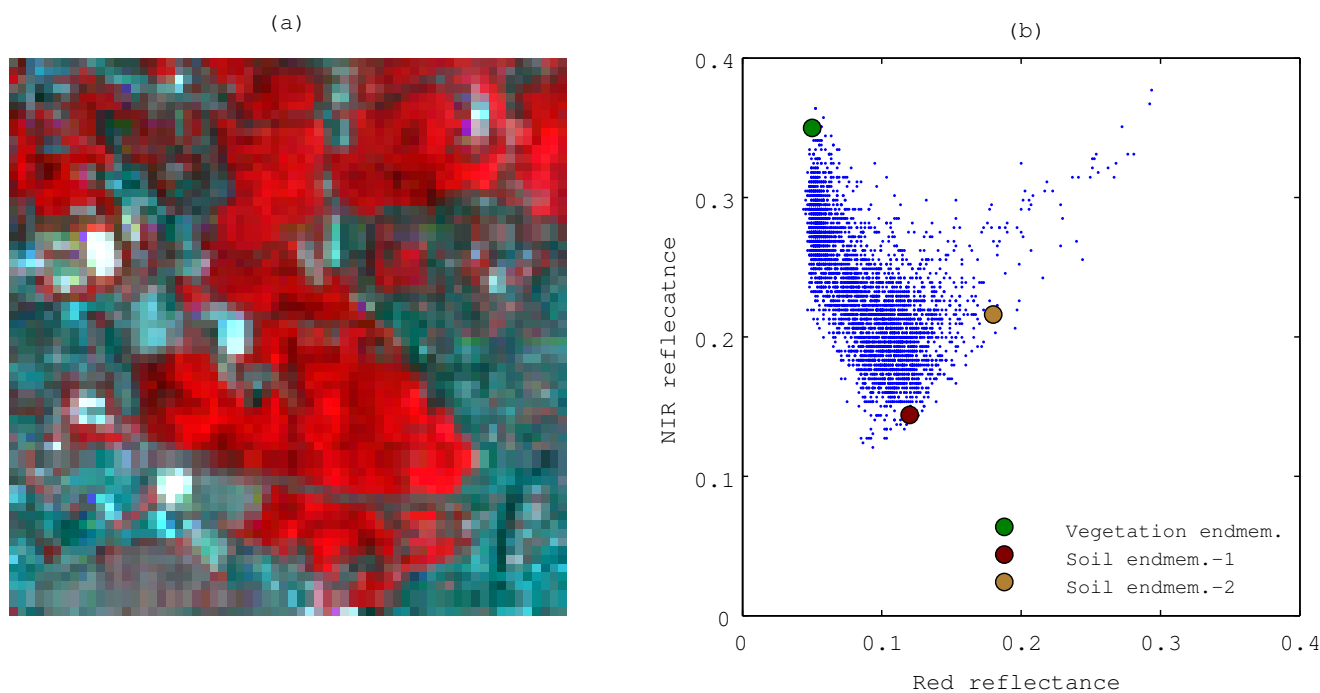


Figure 2. False-color images of the spectral data at several resolution levels used to simulate the scaling effect in the calculation of an averaged FVC.

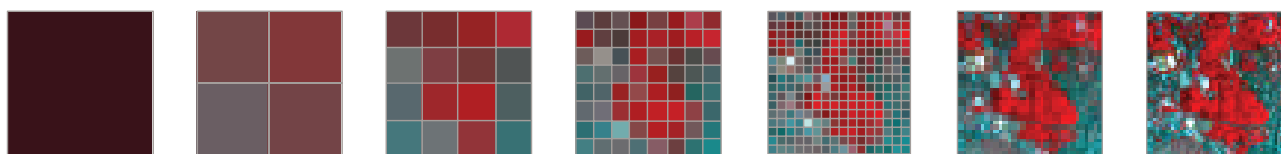
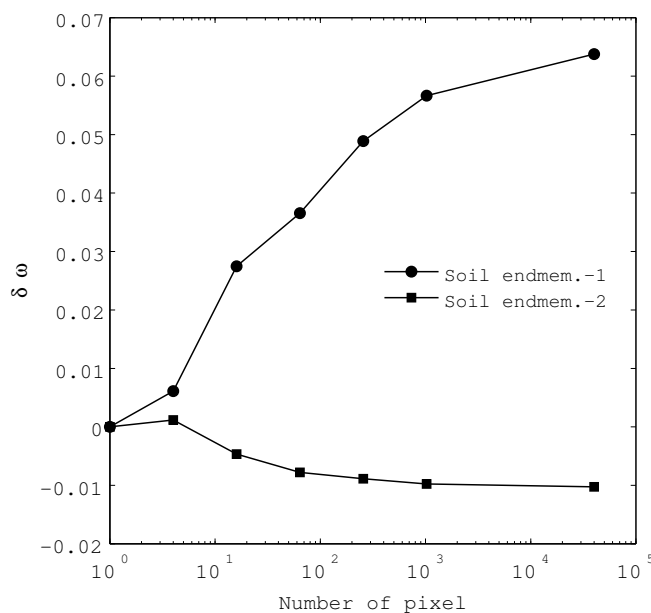


Figure 3. Scaling effects of area-averaged FVC, calculated based on the NDVI-isoline-based LMM as a function of the spatial resolution, using two pairs of endmember spectra. The averaged FVC derived using the vegetation endmember and the soil endmem.-1 spectra is indicated by the filled circles. The averaged FVC derived using the vegetation endmember and soil endmem.-2 spectra is indicated by the filled squares. Increasing and decreasing trends in the averaged FVC depend on the choice of endmember spectra assumed in the model. (The trend also depends on the endmember spectra present over the target fields).



2.3. Resolution Transformation Model

The FVC estimate, $\hat{\omega}$, presented in Equation (5), incurs bias errors if $\hat{\rho}_v \neq \rho_v$ or $\hat{\rho}_s \neq \rho_s$. These discrepancies are the source of the scaling effects. To analyze the scaling effects of $\hat{\omega}$ and the monotonic behavior of the scaling effects as a function of the spatial resolution, we introduced the resolution transformation rule described in our previous work [41]. Resolution transformations are conducted according to a simple rule for pixel partitioning that interconnects the area-averaged values of biophysical parameters at different spatial resolutions. A variable α in the model represents the fraction of a pixel remaining after the partitioning process. The definition of the model is described in detail in [41].

The reflectance spectrum for a pixel k at the j -th resolution level can be expressed as $\rho_{j,k}$. Under the two-endmember assumption, the spectrum can also be expressed as the FVC (true value) for pixel k at the j -th resolution, $\omega_{j,k}$, with endmember spectra for the target field (ρ_v and ρ_s) given by

$$\rho_{j,k} = \omega_{j,k}\rho_v + (1 - \omega_{j,k})\rho_s. \quad (8)$$

The estimated FVC for the k -th pixel at the j -th resolution, $\hat{\omega}_{j,k}$, can be expressed as

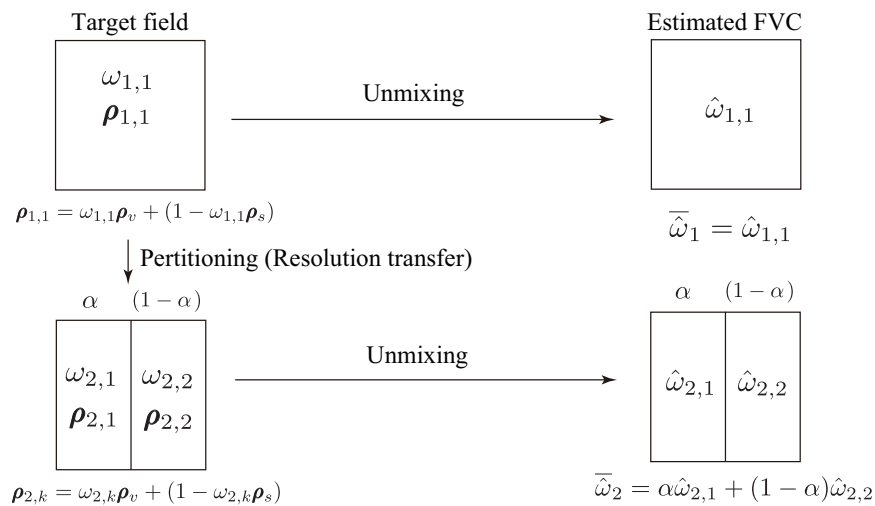
$$\hat{\omega}_{j,k} = \frac{\omega_{j,k} \cdot \det(\Delta\rho, \hat{\rho}_s) + \det(\rho_s, \hat{\rho}_s)}{\omega_{j,k} \cdot \det(\Delta\hat{\rho}, \Delta\rho_s) + \det(\Delta\hat{\rho}, \rho_s)}. \quad (9)$$

The area-averaged FVC values estimated using the algorithm for the j -th resolution level become

$$\bar{\omega}_j = \frac{1}{j} \sum_{k=1}^j \hat{\omega}_{j,k}. \tag{10}$$

Note that the areas of all pixels are equal in an above equation. A set of appropriate weights should be used for area averaging processes if the pixel size is not identical [41]. The variables assumed for the partitioning and unmixing processes are described in Figure 4. In the figure, a target spectrum derived from data at the 1st resolution level ($\rho_{1,1}$) is expressed as a function of the endmember spectra corresponding to the vegetation and non-vegetation coverage over a target field (ρ_v and ρ_s , respectively) and the FVC over the target field ($\omega_{1,1}$). The FVC estimate at the 1st resolution level ($\hat{\omega}_{1,1} = \bar{\omega}_1$) is obtained by unmixing based on the spectrum $\rho_{1,1}$ and the endmember spectra assumed in the model ($\hat{\rho}_v$ and $\hat{\rho}_s$). The resolution transformation is performed by partitioning the data at the first resolution level into two sub-pixels. The partition ratios across the pixel pair are represented by α and $(1 - \alpha)$. The target spectra in each pixel ($\rho_{2,k}$) are functions of the FVC for the pixel ($\omega_{2,k}$) and the endmember spectra (ρ_v and ρ_s). FVC estimates for each pixel at the second resolution level ($\hat{\omega}_{2,k}$) can be obtained by unmixing the target spectra $\rho_{2,k}$ based on the endmember spectra assumed in the model, $\hat{\rho}_v$ and $\hat{\rho}_s$. The area-averaged FVC for the second resolution level is a linear sum of $\hat{\omega}_{2,1}$ and $\hat{\omega}_{2,2}$ with weights α and $(1 - \alpha)$.

Figure 4. Illustration of the variables, the partitioning process, and the unmixing process used to implement a FVC estimate using the isoline-based LMM.



The averaged FVC estimate at the j -th resolution level can be expressed in terms of the sum of the average FVC value at the $(j - 1)$ -th resolution level and the factor $\Delta\bar{\omega}$, according to

$$\bar{\omega}_j = \bar{\omega}_{j-1} + \Delta\bar{\omega}. \tag{11}$$

By substituting 2 into j in Equation (11), $\Delta\bar{\omega}$ can be transformed as follows:

$$\Delta\bar{\omega} = \bar{\omega}_2 - \bar{\omega}_1 = \alpha\hat{\omega}_{2,1} + (1 - \alpha)\hat{\omega}_{2,2} - \hat{\omega}_{1,1}. \tag{12}$$

Recall that the transformation of the spatial resolution can be modeled by repeatedly applying this “unit” resolution transformation from level 1 to 2. $\Delta\bar{\omega}$ in Equation (12) thus becomes a key to analyzing the monotonicity as a function of the spatial resolution. For instance, if the sign of $\Delta\bar{\omega}$ is invariant under the resolution transformation, the average FVC values certainly vary monotonically.

3. Monotonicity of the Area-Averaged FVC

The variable $\Delta\bar{\omega}$ provides a basis for analyzing the monotonicity of the area-averaged FVC. $\Delta\bar{\omega}$ is a function of (1) the endmember spectra used in the model; (2) the target field ($\hat{\rho}_v$, $\hat{\rho}_s$, ρ_v , and ρ_s); and (3) the parameters that vary for each partitioning event (during a resolution transform), such as the true value of the FVC in the data at the second resolution level ($\omega_{2,k}$) or the partition ratio (α). We therefore focus on the sign of $\Delta\bar{\omega}$ and the dependence of the above variables on $\Delta\bar{\omega}$.

3.1. Partial Derivative of $\Delta\bar{\omega}$ with Respect to $\omega_{2,1}$

The sign and dependence of the inputs on $\Delta\bar{\omega}$ were analyzed by deriving the partial derivative of $\Delta\bar{\omega}$ with respect to the FVC for a 1st pixel in the 2nd resolution level, $\omega_{2,1}$, using Equation (12),

$$\frac{\partial\Delta\bar{\omega}}{\partial\omega_{2,1}} = \alpha\frac{\partial\hat{\omega}_{2,1}}{\partial\omega_{2,1}} + (1 - \alpha)\frac{\partial\hat{\omega}_{2,2}}{\partial\omega_{2,1}}, \quad (13)$$

where $\bar{\omega}_1$ is independent of $\omega_{2,1}$. The derivative terms on the right-hand side of Equation (13) can be obtained by taking the derivative of $\hat{\omega}_{2,k}$ (for $k = 1, 2$) with respect to $\omega_{2,k}$,

$$\frac{\partial\hat{\omega}_{2,k}}{\partial\omega_{2,k}} = \frac{\beta}{(\gamma\omega_{2,k} + \phi)^2}, \quad (14)$$

where β , γ , and ϕ are defined by

$$\beta = \det(\Delta\hat{\rho}, \hat{\rho}_s) \cdot \det(\Delta\rho, \rho_s), \quad (15a)$$

$$\gamma = \det(\Delta\hat{\rho}, \Delta\rho), \quad (15b)$$

$$\phi = \det(\Delta\hat{\rho}, \rho_s). \quad (15c)$$

The derivative of $\hat{\omega}_{2,2}$ with respect to $\omega_{2,1}$ can be expressed as

$$\frac{\partial\hat{\omega}_{2,2}}{\partial\omega_{2,1}} = \frac{\partial\hat{\omega}_{2,2}}{\partial\omega_{2,2}} \frac{\partial\omega_{2,2}}{\partial\omega_{2,1}}. \quad (16)$$

The variable $\omega_{1,1}$ can be expressed as

$$\omega_{1,1} = \alpha\omega_{2,1} + (1 - \alpha)\omega_{2,2}. \quad (17)$$

Therefore, $\omega_{2,2}$ can be written as

$$\omega_{2,2} = \frac{\omega_{1,1} - \alpha\omega_{2,1}}{1 - \alpha}. \quad (18)$$

Accordingly, Equation (16) yields the following result (after some rearrangements),

$$\frac{\partial \hat{\omega}_{2,2}}{\partial \omega_{2,1}} = \frac{-\alpha\beta}{(1-\alpha)(\gamma\omega_{2,2} + \phi)^2}. \quad (19)$$

By setting $k = 1$ in Equation (14) and by substituting Equation (19) into Equation (13), the partial derivative of $\Delta\bar{\omega}$ with respect to $\omega_{2,1}$ can be obtained as

$$\frac{\partial \Delta\bar{\omega}}{\partial \omega_{2,1}} = \frac{\alpha\beta}{U_1^2 U_2^2} (U_2^2 - U_1^2), \quad (20)$$

where

$$U_k = \gamma\omega_{2,k} + \phi. \quad (21)$$

3.2. Analysis of $\partial\Delta\bar{\omega}/\partial\omega_{2,1}$

The behavior of $\Delta\bar{\omega}$ can be understood from an analysis of the changes in the sign of $\partial\Delta\bar{\omega}/\partial\omega_{2,1}$. For example, if $\partial\Delta\bar{\omega}/\partial\omega_{2,1}$ changes from negative to positive, the sign of $\Delta\bar{\omega}$ should be positive, regardless of the parameters that determine the spatial characteristics, such as the true FVC, $\omega_{2,k}$, or the pixel partition ratio, α . In this case, the sign depends only on the endmember spectra ($\hat{\rho}_v$, $\hat{\rho}_s$, ρ_v , and ρ_s).

First, the factor β in Equation (20) can be rearranged to give the following expression

$$\beta = \rho_{r,v}\rho_{r,s}\hat{\rho}_{r,v}\hat{\rho}_{r,s} \left(\frac{\rho_{n,v}}{\rho_{r,v}} - \frac{\rho_{n,s}}{\rho_{r,s}} \right) \left(\frac{\hat{\rho}_{n,v}}{\hat{\rho}_{r,v}} - \frac{\hat{\rho}_{n,s}}{\hat{\rho}_{r,s}} \right). \quad (22)$$

Because the four ratios in the parentheses in Equation (22) are equal to the ratio vegetation index (RVI), the two parentheses are inevitably both positive. Thus, Equation (22) is positive as well. The sign of $\partial\Delta\bar{\omega}/\partial\omega_{2,1}$ depends only on the second factor in the right-hand side of Equation (20). The factor may be formulated as $h(\omega_{2,1}, \omega_{2,2})$,

$$\begin{aligned} h(\omega_{2,1}, \omega_{2,2}) &= U_2^2(\omega_{2,2}) - U_1^2(\omega_{2,1}) \\ &= (\gamma\omega_{2,2} + \phi)^2 - (\gamma\omega_{2,1} + \phi)^2. \end{aligned} \quad (23)$$

If $\omega_{2,1} = \omega_{2,2}$, the function $h(\omega_{2,1}, \omega_{2,2})$, $\partial\Delta\bar{\omega}/\partial\omega_{2,1}$, and $\Delta\bar{\omega}$ are equal to zero, then the FVC is scale-invariant. Likewise, if $\gamma = 0$, the above function will be identical to 0, hence, a certain relationship is guaranteed between the modeled and true endmember spectra, represented by the following expression,

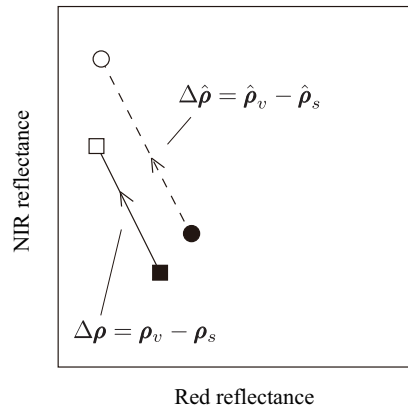
$$\det(\Delta\hat{\rho}, \Delta\rho) = 0. \quad (24)$$

Equation (24) indicates that a vector spanned by the assumed endmember spectra ($\Delta\hat{\rho}$) necessarily becomes parallel to the vector spanned by the true endmember spectra ($\Delta\rho$), as illustrated in Figure 5. Empty and filled squares represent the true vegetation and non-vegetation endmember spectra, respectively. Similarly, the circular symbols indicate the vegetation and non-vegetation endmember spectra, respectively, assumed in the algorithm.

For $\omega_{2,1} \neq \omega_{2,2}$ and $\gamma \neq 0$, however, the function $h(\omega_{2,1}, \omega_{2,2})$ is not equal to zero, and the sign of the function depends on all variables. In this case, Equation (23) can be expressed as

$$h(\omega_{2,1}, \omega_{2,2}) = -2\gamma^2(\omega_{2,1} - \omega_{2,2}) \left(\frac{\omega_{2,2} + \omega_{2,1}}{2} + \frac{1}{\zeta - 1} \right), \quad (25)$$

Figure 5. Illustration of the relationship between the vectors describing the true endmember spectra and the assumed endmember spectra ($\Delta\rho$ and $\Delta\hat{\rho}$) in the red–NIR reflectance space. Empty and filled squares indicate the vegetation and non-vegetation endmember spectra in the target field, and empty and filled circles indicate the assumed endmember spectra in the LMM. When the two vectors are parallel, scaling effects are not observed in the average FVC.



where

$$\zeta = \frac{\det(\rho_v, \Delta\hat{\rho})}{\det(\rho_s, \Delta\hat{\rho})}. \tag{26}$$

A geometrical interpretation of the variable ζ is provided in Section 4. The factor ζ determines the sign of $h(\omega_{2,1}, \omega_{2,2})$ as follows. The sign of $h(\omega_{2,1}, \omega_{2,2})$ can be readily determined once the following information is known. The range of $(\omega_{2,1} + \omega_{2,2})/2$ (the last factor in Equation (25)) becomes

$$0 \leq \frac{\omega_{2,1} + \omega_{2,2}}{2} \leq 1. \tag{27}$$

Within this range, the sign of $h(\omega_{2,1}, \omega_{2,2})$, namely the sign of $\partial\Delta\bar{\omega}/\partial\omega_{2,1}$, can be determined from ζ as follows. If $\zeta > 1$, the last parenthesis in Equation (25) will be positive. Then $\partial\Delta\bar{\omega}/\partial\omega_{2,1}$ will vary from positive to negative as a function of $\omega_{2,1}$.

$$\text{If } \zeta > 1, \quad \frac{\partial\Delta\bar{\omega}}{\partial\omega_{2,1}} \begin{cases} > 0 & (\omega_{2,1} < \omega_{2,2}), \\ = 0 & (\omega_{2,1} = \omega_{2,2}), \\ < 0 & (\omega_{2,1} > \omega_{2,2}). \end{cases} \tag{28}$$

If $0 \leq \zeta < 1$, the last parenthesis in Equation (25) will be negative, hence the sign of $\partial\Delta\bar{\omega}/\partial\omega_{2,1}$ will vary from negative to positive as follows.

$$\text{If } 0 \leq \zeta < 1, \quad \frac{\partial\Delta\bar{\omega}}{\partial\omega_{2,1}} \begin{cases} < 0 & (\omega_{2,1} < \omega_{2,2}), \\ = 0 & (\omega_{2,1} = \omega_{2,2}), \\ > 0 & (\omega_{2,1} > \omega_{2,2}). \end{cases} \tag{29}$$

The sign of $\partial\Delta\bar{\omega}/\partial\omega_{2,1}$ for $\zeta < 0$, however, does not change monotonically with $\omega_{2,1}$ because the sign of the last factor in Equation (25) cannot be unique (dependent on $\omega_{2,1}$). Finally, if $\zeta = 1$, which corresponds to the case of $\gamma = 0$, the average FVC will be independent of the spatial resolution.

3.3. Behavior of $\Delta\bar{\omega}$

The sign and dependence of the input variables on $\Delta\bar{\omega}$ can be summarized as

$$\Delta\bar{\omega} \begin{cases} \leq 0, & (\zeta > 1), \\ = 0, & (\zeta = 1), \\ \geq 0, & (0 \leq \zeta < 1), \\ \text{the sign is variable,} & (\zeta < 0). \end{cases} \tag{30}$$

Consequently, the magnitude of the relationship between $\bar{\omega}_2$ and $\bar{\omega}_1$ can be written as

$$\bar{\omega}_2 \begin{cases} \leq \bar{\omega}_1, & (\zeta > 1), \\ = \bar{\omega}_1, & (\zeta = 1), \\ \geq \bar{\omega}_1, & (0 \leq \zeta < 1), \\ \text{the relation is variable,} & (\zeta < 0). \end{cases} \tag{31}$$

Note that if ζ is equal to or greater than zero, the relationship between $\bar{\omega}_2$ and $\bar{\omega}_1$ is independent of the true value of the fractional abundances of the endmember spectra ($\omega_{2,k}$) or on the fractional areas by which one pixel is divided into two (α). On one hand, the relationship depends only on the spectra of the endmember components assumed in the algorithm and the true spectra of the target field ($\hat{\rho}_v, \hat{\rho}_s, \rho_v$, and ρ_s).

3.4. Monotonicity of the Area-Averaged FVC

As derived in the previous subsection, the sign of the factor $\Delta\bar{\omega}$ is invariant during any resolution transform if the endmember spectra satisfy certain conditions ($\zeta \geq 0$). In other words, the relationship between the FVC values before and after partitioning should be invariant under each step of the resolution transform. The relationship results in monotonic changes in the average FVC for $\zeta \geq 0$ as a function of the resolution transform sequence. Recall that the resolution transform sequence generated by the repeated application of a simple partitioning rule is referred to as a “resolution class”. The findings from the derivation presented in this section are summarized in the following theorems (under the two-endmember assumption).

Theorem 1 Within a single resolution class, the area-averaged FVC values change monotonically as a function of the spatial resolution if $\zeta \geq 0$.

When this is the case,

Theorem 2 The area-averaged FVC values follow a trend determined by ζ such that estimation of the FVC is a non-increasing function if $\zeta > 1$ or a non-decreasing function if $0 \leq \zeta < 1$.

On the one hand, the average FVC values can change non-monotonically for $\zeta < 0$ because the relationship between the average FVC values at any two resolutions will vary.

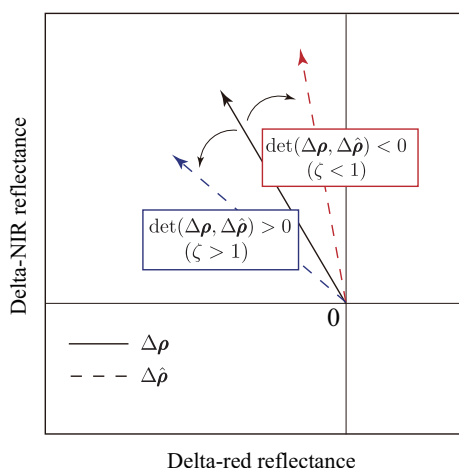
4. Geometrical Relationship between ζ and the Endmember Spectra over the Delta Reflectance Space

The variable ζ may be interpreted geometrically as a factor that determines the monotonic behavior within the scope of monotonicity ($\zeta \geq 0$). By applying Equation (26), we can derive equations that comprehensively describe the relation between ζ and the endmember spectra as follows:

$$\det(\Delta\rho, \Delta\hat{\rho}) \begin{cases} > 0 & (\zeta > 1), \\ = 0 & (\zeta = 1), \\ < 0 & (\zeta < 1). \end{cases} \tag{32}$$

where $\det(\Delta\rho, \Delta\hat{\rho})$ represents the determinant of a matrix consisting of the vectors $\Delta\rho$ and $\Delta\hat{\rho}$. The geometrical relationship is described over a delta-reflectance space in which the x -axis represents the difference between the red reflectance of the vegetation and non-vegetation classes (delta-red reflectance). The y -axis in this space represents the delta-NIR reflectance (Figure 6).

Figure 6. A geometrical interpretation of the variable ζ , the endmember spectra in the model, $\Delta\hat{\rho}$ (colored dashed arrows), and the target field, $\Delta\rho$ (a solid arrow). If $\zeta > 1$, the determinant, $\det(\Delta\rho, \Delta\hat{\rho})$, becomes positive, indicating that the vector over the endmember spectra to be estimated, $\Delta\hat{\rho}$, should be described in regions of the left-hand side of the vector corresponding to the difference between the true vectors, $\Delta\rho$ (a solid vector), indicated in blue. That is, $\Delta\hat{\rho}$ may be expressed as a vector rotated counterclockwise relative to $\Delta\rho$. Similarly, if $0 \leq \zeta < 1$, the determinant is less than unity and $\Delta\hat{\rho}$ may be expressed as a vector rotated clockwise relative to $\Delta\rho$.



If $\zeta > 1$, then the determinant, $\det(\Delta\rho, \Delta\hat{\rho})$ becomes positive, indicating that the vector expressed over the basis of the endmember spectra to be estimated, $\Delta\hat{\rho}$, should be described in regions of the left-hand side of the vector corresponding to the difference between the true vectors, $\Delta\rho$ (the solid vector in Figure 6), indicated by a blue dashed vector over the delta-red and delta-NIR reflectance space. In other words, $\Delta\hat{\rho}$ may be expressed as a vector rotated counterclockwise from $\Delta\rho$. Similarly, if $\zeta < 1$, the determinant is less than unity, and $\Delta\hat{\rho}$ may be expressed as a vector rotated clockwise relative to $\Delta\rho$,

as illustrated by the red dashed line in Figure 6. Note that these interpretations fall within the limited cases that display monotonicity in the averaged FVC ($\zeta \geq 0$).

Next, we present a set of numerical examples that demonstrate the relationship between the monotonicity (ζ value) and the endmember spectra (including cases in which non-monotonicity ($\zeta < 0$) holds) over the delta-reflectance space. The factor ζ is explicitly a function of ρ_v and ρ_s and $\Delta\hat{\rho}$, given by $\hat{\rho}_v$ and $\hat{\rho}_s$. In this simulation, two vectors, $\Delta\hat{\rho}$ and $\Delta\rho$, were considered (in Equation (32)). $\Delta\rho$ was held constant, and the vector $\Delta\hat{\rho}$ was varied from 0 to 2π in 0.10 radian increments. The origins of the two key vectors $\Delta\rho$ and $\Delta\hat{\rho}$ have been shifted relative to the origin of the coordinate system for comparison purpose. The lengths of these vectors were set to be equal to facilitate interpretation. Note that the lengths do not affect monotonicity trend. An example of the results is shown in Figure 7. The black arrows indicate $\Delta\rho$ and the gray arrows indicate ρ_v and ρ_s . The colored arrows indicate $\Delta\hat{\rho}$ for the respective trends: green arrows correspond to the non-decreasing trends of the averaged FVC ($0 \leq \zeta < 1$). Red arrows fall into the range of non-increasing ($\zeta > 1$). Blue arrows indicate the non-monotonic case ($\zeta < 0$). In Figure 7, $\Delta\rho$, denoted by the black arrow, is located just on the boundary of two regions (indicated by the red and green arrows). Note that the boundaries between the trends (indicated by the arrows of different colors) are determined by the three vectors, $\Delta\rho$, ρ_v , and ρ_s , which match the representation of Figure 6.

Figure 7. An example numerical demonstrations of the relationships between the endmember spectra and the monotonic behavior of the area-averaged FVC. $\Delta\hat{\rho}$ was varied from 0 to 2π in 0.10 radian increments. The initial point and the length of the vectors were assumed to be (0, 0) and 0.25, respectively. $\Delta\rho$ is indicated by black arrows, and the vector defined by the assumed endmember spectra, $\Delta\hat{\rho}$, is indicated by the colored arrows. Gray arrows indicate ρ_v and ρ_s . The vectors indicated in green correspond to non-decreasing trends in the averaged FVC ($0 \leq \zeta < 1$). The red arrows indicate that ζ falls into the class of non-increasing functions ($\zeta > 1$). The blue arrows indicate non-monotonic case ($\zeta < 0$).

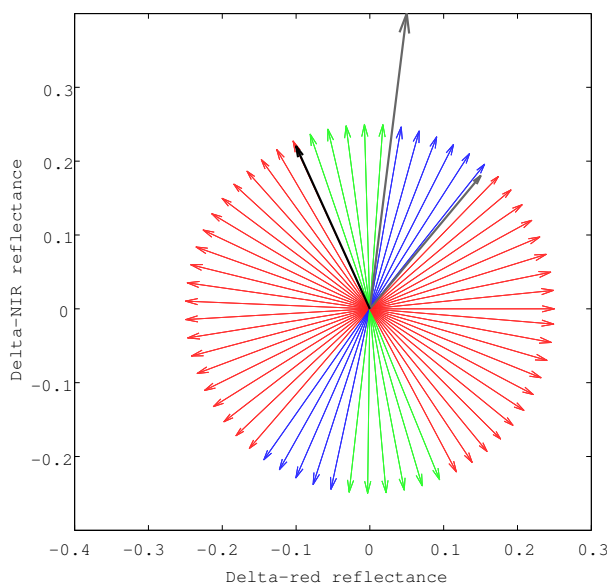


Figure 8. Results of numerical demonstration of the relationship between the endmember spectra and the monotonic behavior of the area-averaged FVC. Nine vector variations corresponding to different endmember spectra $\Delta\rho$ were considered, as listed in (a–i) in Table 2. The vectors indicated in green correspond to non-decreasing trends in the averaged FVC ($0 \leq \zeta < 1$). The red arrows indicate that ζ falls into the class of non-increasing functions ($\zeta > 1$). The blue arrows indicate non-monotonic case ($\zeta < 0$). The results show the influence of the changes in $\Delta\rho$ on the relation. Namely, angular ranges of each colored vector (trends in averaged FVC along spatial resolution) vary with $\Delta\rho$.

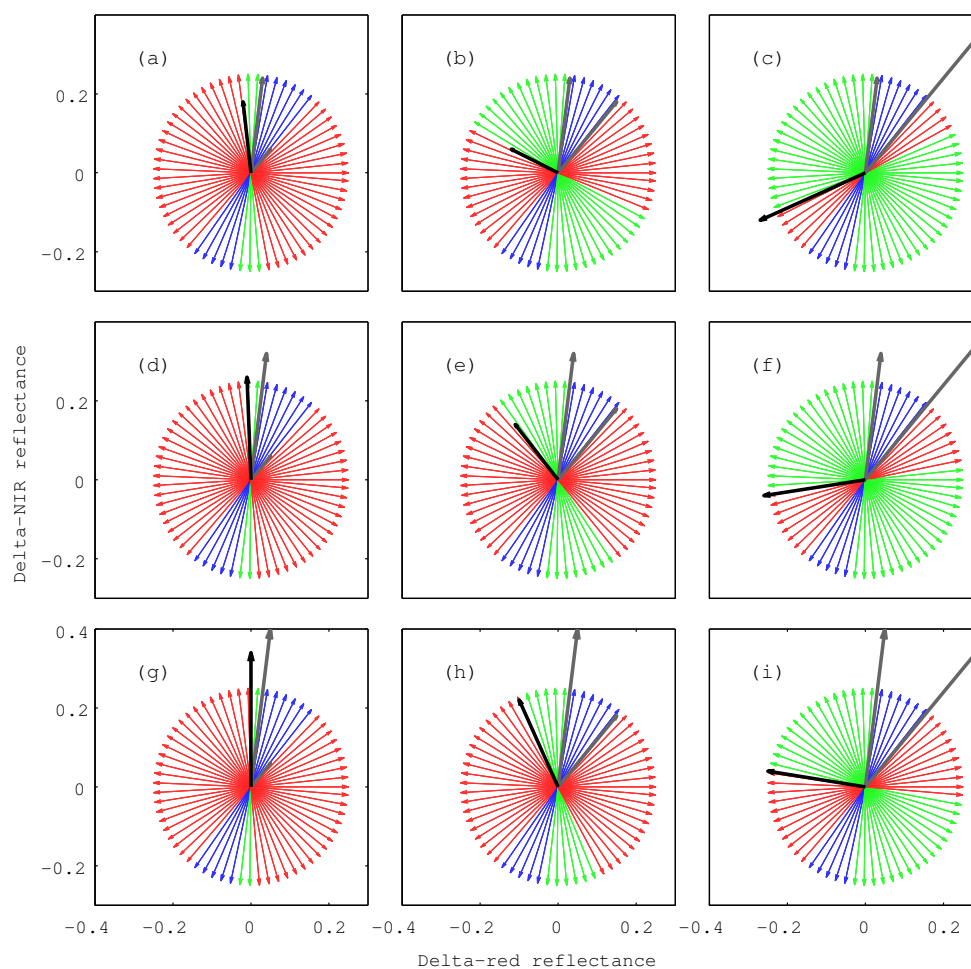


Figure 8 shows the vector $\Delta\rho = (\Delta\rho_r, \Delta\rho_n)$ in a vector chart for all nine cases of the endmember spectra summarized in Table 2. The results show the influence of the change in $\Delta\rho$ on the relation. The results show that the delta-reflectance ranges of the decreasing and increasing trends depended significantly on the reflectances of the non-vegetation endmember. For instance, although no obvious differences are observed among the results shown in Figure 8(a,d,g) for the different vegetation endmember spectra assumed, the contribution of the non-decreasing (green arrows) components increased with the red reflectance in the non-vegetation endmember, as shown in Figure 8(a–c). The blue arrows corresponding to the non-monotonic behavior are situated between ρ_v and ρ_s , indicated by the gray arrows (Figure 8). Non-monotonicity in the averaged FVC is rarely observed because the angle $\Delta\hat{\rho}$ relative to the x -axis often exceeds that of ρ_v ; however, if the non-vegetation endmember reflects

extremely lower radiances (for example, in coastal and watershed regions) $\Delta\hat{\rho}$ may fall among the blue vectors, as shown in Figure 8(a,d,g). Even if $\Delta\hat{\rho}$ points in the opposite direction ($-\Delta\hat{\rho}$), the ζ value is invariant under Equation (26). This property results in a point reflection of $\Delta\hat{\rho}$ with respect to the monotonicity, as shown in Figure 8.

Table 2. Endmember spectra in the red and NIR, corresponding to vegetation ($\rho_{v,r}$ and $\rho_{v,n}$) and non-vegetation ($\rho_{s,r}$ and $\rho_{s,n}$) coverage, and the differences between the endmember reflectances of each band ($\Delta\rho_r$ and $\Delta\rho_n$) used in the numerical demonstration.

	(a)	(b)	(c)	(d)	(e)	(f)	(g)	(h)	(i)
$\rho_{v,r}$	0.03	0.03	0.03	0.04	0.04	0.04	0.05	0.05	0.05
$\rho_{v,n}$	0.24	0.24	0.24	0.32	0.32	0.32	0.4	0.4	0.4
$\rho_{s,r}$	0.05	0.15	0.30	0.05	0.15	0.30	0.05	0.15	0.30
$\rho_{s,n}$	0.06	0.18	0.36	0.06	0.18	0.36	0.06	0.18	0.36
$\Delta\rho_r$	-0.02	-0.12	-0.27	-0.01	-0.11	-0.26	0	-0.10	-0.25
$\Delta\rho_n$	0.18	0.06	-0.12	0.26	0.14	-0.04	0.34	0.22	0.04

5. Validation of the Analytical Implications

In this section, we introduce a set of numerical experiments in an effort to validate the results derived here in a practical application. Equation (31) implies an important fact, that the FVC values produced under a resolution transformation do not display variations for $\zeta = 1$. This result implies that the endmember spectra assumed in the algorithm provide FVC values that are less sensitive to scaling effects. In the section below, the numerical experiments are explained to provide evidence for a practical demonstration that demonstrates the utility of our analysis.

The major difficulties associated with this validation lie in the difficulty of estimating ζ using actual satellite data. ζ is a function of the “true” endmember spectra for both vegetation and non-vegetation surfaces, and a rigorous estimation/determination of these endmember spectra is generally impossible. Therefore, we circumvent this difficulty by effectively varying the value of ζ according to the following procedure.

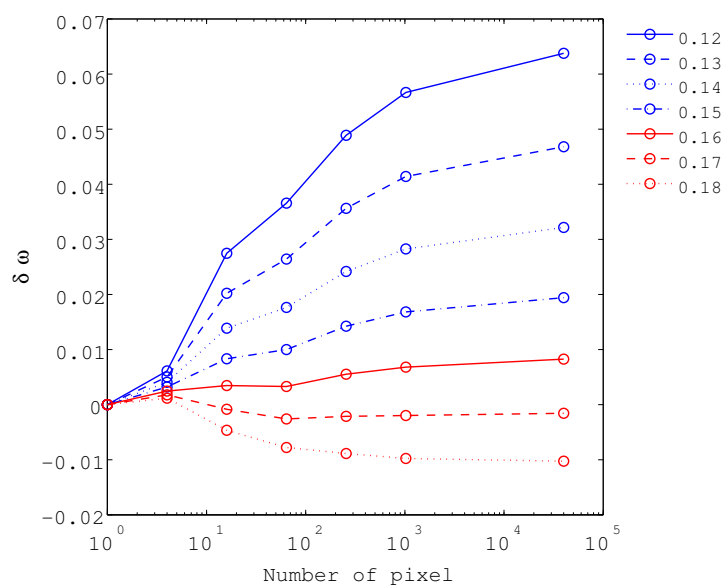
The satellite data presented in Figure 1 were used to simulate the FVC values at various spatial resolution levels (for a total of seven resolution cases). In this experiment, we processed the data using different pairs of assumed endmember spectra. The non-vegetation endmember spectra ($\hat{\rho}_s$) were varied as shown in Table 3, whereas the spectrum of the vegetation endmember was held fixed at (0.05, 0.35), the spectrum presented in Figure 1. The variations on $\hat{\rho}_s$ were implemented to effectively introduce variations in ζ . Note that the estimation of ζ is impossible because the “true” endmembers are unknown; however, the variations in $\hat{\rho}_s$ most likely shift the value of ζ , as anticipated.

Figure 9 shows the scaling effects in the FVC values as a function of the endmember spectra assumed. The figure clearly indicates that (1) the trend in the FVC values as a function of the spatial resolution changes as the value of ζ changes (ζ depends on $\hat{\rho}_s$ in this experiment); and (2) FVC is less sensitive to ζ for some pairs of endmember spectra, which agrees well with the implications of the results derived above.

Table 3. Red and NIR reflectances of the assumed non-vegetation endmember spectra in the validation experiment.

Red reflectance	0.12	0.13	0.14	0.15	0.16	0.17	0.18
NIR reflectance	0.14	0.16	0.17	0.18	0.19	0.20	0.22

Figure 9. Scaling effects in the FVC, determined for various endmember spectra corresponding to the non-vegetation surface (Table 3) assumed in the algorithm.



6. Maximum Variations Induced by the Scaling Effects Observed in the Averaged FVC

6.1. Derivation of the Maximum Variations

The magnitude of the scaling effects depend on the true FVC value within a target area under a fixed pair of assumed endmember spectra. In this section, we focus on the maximum scaling effects in the FVC as a function of the true FVC. The magnitude of the scaling effects is measured as the difference between the two extreme resolutions (the lumped and distributed cases). This difference can be considered to provide the bounds on the errors resulting from the scaling effects when the assumed endmember spectra meet the conditions for monotonicity, as described in Theorem 1 ($\zeta \geq 0$).

The focus of this discussion is on the differences between the FVC values at the coarsest and finest resolution. Note that the finest resolution corresponds to the case in which all pixels are composed of only one type of surface. In this case, the spectrum of each pixel may be represented by a single endmember spectrum (either vegetation or non-vegetation). Comparing the two extremes, the scaling effects in the FVC may be defined by

$$\Delta \bar{\hat{\omega}}_{1 \rightarrow f} = \hat{\omega}_1 - \bar{\hat{\omega}}_{(f)}, \tag{33}$$

where $\bar{\hat{\omega}}_{(f)}$ is an area-averaged FVC value at the finest resolution (distributed case), with the subscript

f indicating the “finest” resolution. $\bar{\omega}_{(f)}$ is defined by

$$\bar{\omega}_{(f)} = \omega \hat{\omega}_{(v)} + (1 - \omega) \hat{\omega}_{(s)}, \tag{34}$$

where $\hat{\omega}_{(v)}$ and $\hat{\omega}_{(s)}$ represent the FVC estimates for the vegetation and non-vegetation endmember spectra, expressed by

$$\hat{\omega}_{(v)} = \frac{v_v - \hat{v}_s}{(1 - \hat{\eta})(v_v - \hat{v}_v) + \hat{v}_v - \hat{v}_s}, \tag{35}$$

$$\hat{\omega}_{(s)} = \frac{v_s - \hat{v}_s}{(1 - \hat{\eta})(v_s - \hat{v}_v) + \hat{v}_v - \hat{v}_s}, \tag{36}$$

with the definitions of

$$v_v = \frac{\rho_{v,n} - \rho_{v,r}}{\rho_{v,n} + \rho_{v,r}}, \tag{37}$$

$$v_s = \frac{\rho_{s,n} - \rho_{s,r}}{\rho_{s,n} + \rho_{s,r}}. \tag{38}$$

In order to derive the maximum of $\Delta \bar{\omega}_{1 \rightarrow f}$ as a function of the true FVC, we consider a partial derivative of $\Delta \bar{\omega}_{1 \rightarrow f}$ with respect to ω , that is,

$$\frac{\partial \Delta \bar{\omega}_{1 \rightarrow f}}{\partial \omega} = \frac{\partial \hat{\omega}_1}{\partial \omega} - \frac{\partial \bar{\omega}_{(f)}}{\partial \omega}. \tag{39}$$

The first term of Equation (39) becomes

$$\frac{\partial \hat{\omega}_1}{\partial \omega} = \frac{\det(\Delta \hat{\rho}, \hat{\rho}_s) \det(\Delta \rho, \rho_s)}{[\det(\Delta \hat{\rho}, \Delta \rho) \omega + \det(\Delta \hat{\rho}_s)]^2}. \tag{40}$$

The second term of Equation (39) becomes

$$\frac{\partial \bar{\omega}_{(f)}}{\partial \omega} = \frac{v_v - \hat{v}_s}{(1 - \hat{\eta})(v_v - \hat{v}_v) + \hat{v}_v - \hat{v}_s} - \frac{v_s - \hat{v}_s}{(1 - \hat{\eta})(v_s - \hat{v}_v) + \hat{v}_v - \hat{v}_s}. \tag{41}$$

$\Delta \bar{\omega}_{1 \rightarrow f}$ reaches a maximum when

$$\frac{\partial \Delta \bar{\omega}_{1 \rightarrow f}}{\partial \omega} = 0. \tag{42}$$

Solving the system of Equations (39), (40), (41), and (42) for ω yields

$$\omega = \frac{1}{1 - \zeta} \pm \frac{C}{1 - \zeta}, \tag{43}$$

where

$$C = \frac{1}{\det(\rho_s, \Delta \hat{\rho})} \sqrt{\frac{\det(\hat{\rho}_s, \Delta \hat{\rho}) \det(\rho_s, \Delta \rho)}{\hat{\omega}_v - \hat{\omega}_s}}, \tag{44}$$

The coefficient C is always positive because all determinants in Equation (44) are positive, given that the following four relationships hold; $v_v > v_s$, $\hat{v}_v > \hat{v}_s$, $\hat{v}_v > v_s$, and $\hat{\omega}_v > \hat{\omega}_s$. If ζ exceeds unity in Equation (43), the two terms are negative, and the negative sign must be selected in Equation (43)

by noting the range of FVC values, ($0 \leq \omega \leq 1$). Similarly, if ζ is less than unity, the first term in Equation (43) exceeds unity. As a result, the negative sign must be selected. In summary, the FVC value (ω_{max}) that provides the maximum value of $\Delta\bar{\omega}_{1 \rightarrow f}$ is

$$\omega_{max} = \frac{1 - C}{1 - \zeta}. \tag{45}$$

The maximum of $\Delta\bar{\omega}_{1 \rightarrow f}$, denoted $\Delta\bar{\omega}_{1 \rightarrow f}(\omega_{max})$, can be derived by substituting Equation (45) into Equation (33), which implicitly includes ω as a parameter. The result is a ratio of quadratic forms in the variable $\mathbf{x} = {}^t(1 - \zeta, 1 - C)$,

$$\Delta\bar{\omega}_{1 \rightarrow f}(\omega_{max}) = {}^t\mathbf{x}\mathbf{A}\mathbf{x} / {}^t\mathbf{x}\mathbf{B}\mathbf{x}, \tag{46}$$

where

$$\mathbf{A} = \begin{bmatrix} \det(\boldsymbol{\rho}_s, \hat{\boldsymbol{\rho}}_s) & [\det(\Delta\boldsymbol{\rho}, \hat{\boldsymbol{\rho}}_s) - \det(\Delta\hat{\boldsymbol{\rho}}, \boldsymbol{\rho}_s)(\hat{\omega}_{(v)} + \hat{\omega}_{(s)})]/2 \\ [\det(\Delta\boldsymbol{\rho}, \hat{\boldsymbol{\rho}}_s) - \det(\Delta\hat{\boldsymbol{\rho}}, \boldsymbol{\rho}_s)(\hat{\omega}_{(v)} + \hat{\omega}_{(s)})]/2 & \det(\Delta\hat{\boldsymbol{\rho}}, \Delta\boldsymbol{\rho})(\hat{\omega}_{(v)} + \hat{\omega}_{(s)}) \end{bmatrix}, \tag{47}$$

$$\mathbf{B} = \begin{bmatrix} \det(\Delta\hat{\boldsymbol{\rho}}, \boldsymbol{\rho}_s) & \det(\Delta\hat{\boldsymbol{\rho}}, \Delta\boldsymbol{\rho})/2 \\ \det(\Delta\hat{\boldsymbol{\rho}}, \Delta\boldsymbol{\rho})/2 & 0 \end{bmatrix}. \tag{48}$$

6.2. Numerical Validation

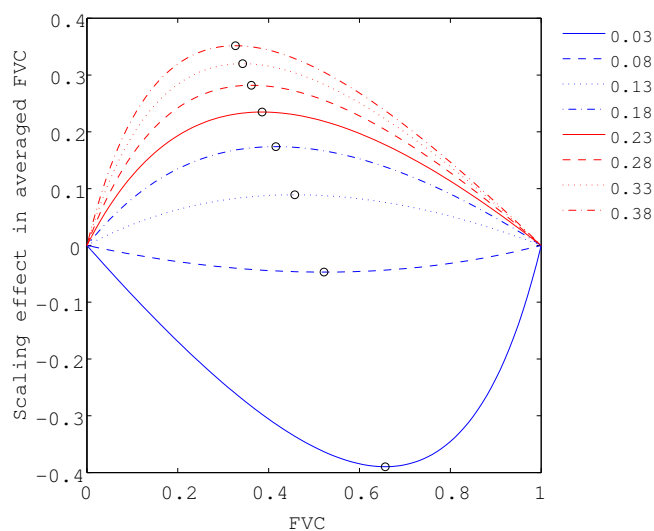
The results derived to express the maximum variations in FVC in terms of the scaling effects were validated by numerical experiments. The variables ω_{max} and $\Delta\bar{\omega}_{1 \rightarrow f}(\omega_{max})$ were computed for the set of endmember spectra listed in Table 4. The non-vegetation endmember spectrum was varied along the soil line. The slope and offset of the assumed soil line are 1.2 and 0.0, respectively. The red reflectance was varied from 0.03 to 0.38 at intervals of 0.05 (total of eight cases).

Table 4. True endmember spectra for the vegetation ($\boldsymbol{\rho}_v$) and non-vegetation ($\boldsymbol{\rho}_s$) surfaces (over a target field), and assumed endmember spectra for vegetation ($\hat{\boldsymbol{\rho}}_v$) and non-vegetation ($\hat{\boldsymbol{\rho}}_s$) surfaces in the FVC retrieval algorithm during the numerical simulations.

	$\boldsymbol{\rho}_v$	$\boldsymbol{\rho}_s$	$\hat{\boldsymbol{\rho}}_v$	$\hat{\boldsymbol{\rho}}_s$
Red reflectance	0.05	0.10	0.05	0.03~0.38 at 0.05 (8 cases)
NIR reflectance	0.40	0.12	0.36	NIR=1.2Red

Simulations were conducted according to the following steps. First, the values of $\Delta\bar{\omega}_{1 \rightarrow f}(\omega)$ were computed by varying the true FVC from zero to unity for each of the eight cases involving soil endmember spectra assumed in the retrieval algorithms. The scaling effects were then plotted as a function of the true FVC value for the eight cases involving different soil endmembers. The results are indicated by the eight distinct lines in Figure 10. In the second step, the variables ω_{max} and $\Delta\bar{\omega}_{1 \rightarrow f}(\omega_{max})$ were computed from Equations (45) and (46) separately based on the results from the previous step. The computed pairs of ω_{max} and $\Delta\bar{\omega}_{1 \rightarrow f}(\omega_{max})$ (denoted by the empty circles) were then plotted along with the simulated results in the figure. The figure clearly shows the validity of the derived results (ω_{max} and $\Delta\bar{\omega}_{1 \rightarrow f}(\omega_{max})$).

Figure 10. Numerical demonstration of ω_{max} and $\Delta\bar{\omega}_{1\rightarrow f}(\omega_{max})$. The values of $\Delta\bar{\omega}_{1\rightarrow f}$ were computed over the domain of true FVC values (from zero to unity) using the eight endmember sets listed in Table 4. The non-vegetation endmember spectrum was varied over the red reflectance range from 0.03 to 0.38 in increments of 0.05, and the slope of the soil line was assumed to be 1.2. The red reflectance in the non-vegetation endmember are identified based on the colors and lines. The variables ω_{max} and $\Delta\bar{\omega}_{1\rightarrow f}(\omega_{max})$ are plotted over the results and are denoted by empty circles.



7. Discussion

Previous studies of the scaling effects attempted to derive appropriate error bounds and to develop algorithms for correcting scaling effects [33,39,49–51]. In this sense, the motivation and objectives of the present study are somewhat similar to previous studies; however, the framework of the analysis presented here differ substantially from the previous studies, which focused on the uncertainties associated with parameter retrieval at the two extreme resolutions (finest and coarsest) due to variations in the spectral measurements at each point within a pixel. The pixel-scale reflectance was held constant at all resolutions. In their work, the endmember spectral ranges (spectral variations) were parameters that eventually determined the error bounds based on the characteristics of the function (e.g., convex or concave) [39]. By contrast, both the spectral and spatial contributions to the scaling effects were investigated in this study. By parameterizing both contributions for a given set of spectral and spatial variables, the monotonicity of the FVC could be determined, leading to a discussion of the error bounds. Note that the resolution transformation model introduced in our previous study enabled us to perform an analysis over the entire set of resolution cases.

This study was conducted as an extension of our previous work, in which we analyzed the scaling effects in the calculation of area-averaged NDVI (the monotonicity of the NDVI) [41]. If the averaged FVC shifts monotonically within a given resolution class (ζ equals to or exceeds zero), the FVC values at either extreme resolution (the coarsest and finest resolution levels) are either the maximum or minimum values. The reasoning behind this conclusion is as follows: the extreme resolutions belong to the same resolution class, and any resolution case certainly belongs to at least one of the resolution classes;

therefore, the FVC values strictly specify the error bounds on the scaling effects in an FVC estimate caused by changes in the spatial resolution.

In light of the findings associated with the error bounds discussed above, we further derived the maximum difference between FVC values at the two extreme resolution levels as a function of a true FVC value for a fixed set of true and assumed endmember spectra. We derived the expression for the maximum difference as a function of both the “true” endmember spectra and the “assumed” spectra in the algorithm.

The scope of practical applications that lend themselves to the findings of this study is limited due to the difficulties associated with accurately estimating the “true” endmember spectra in a target area. Nevertheless, the estimations of the error bounds in FVC calculations are only one type of application; any technique may be used to measure the ranges over which the true endmember spectra vary across the red–NIR reflectance space. Such approaches can lead to uncertainty in the estimates of the averaged FVC values across spectral data collected at multiple resolutions. One often encounters this type of application in the context of long-term observations of biophysical variables by multiple sensors, where the inter-sensor calibration between sensors of two different resolutions plays an important role. Further studies are needed to explore this possibility.

8. Conclusions

This work investigated the mechanism underlying the scaling effects in an fraction of vegetation cover (FVC) retrieval algorithm using an NDVI-isoline-based linear mixture model (LMM) in an extension of our previous analysis (which treated the scaling effects on NDVI). The analysis was performed by focusing on the monotonicity of area-averaged FVC calculations as a function of the spatial resolution. The assumption of a two-endmember LMM facilitated the analytical treatment, which was found to be consistent with our previous investigations of NDVI scaling effects. Interestingly, the monotonic behavior of the FVC was somewhat different from that observed in NDVI calculations, even though the FVC algorithm used NDVI as a condition. The NDVI changes monotonically within a resolution class under the two-endmember LMM, whereas the FVC computed by the NDVI-isoline-based LMM does not necessarily change monotonically. This non-monotonic behavior occurs when the endmember spectra satisfies a certain condition. In other words, the NDVI and FVC may behave differently regarding their monotonic aspect, which is one of the findings of this study.

The condition of monotonicity was determined by the factor ζ , which is a function of the “true” vegetation and non-vegetation endmember spectra over a target field and the endmember spectra “assumed” in the algorithm. Remarkably, this factor was independent of the true value of the FVC over a target field. It means that distribution and fraction of the endmember components do not affect the monotonic behavior. This clearly suggests that the monotonicity was determined only by the two sets of endmember spectra. If $\zeta \geq 0$, then the average FVC varied monotonically with the spatial resolution within a resolution class (generated by repeated application of a simple partitioning rule). In contrast, the average FVC varied non-monotonically for $\zeta < 0$.

If FVC varies monotonically ($\zeta \geq 0$), the error bounds on the FVC due to the scaling effects may be determined from the FVC values at the extreme resolution levels for a target field consisting of two

endmembers (vegetation and non-vegetation). In contrast, if the FVC varies non-monotonically ($\zeta < 0$), it becomes difficult to determine the error bounds because it is not possible to identify the positions of the maximum and minimum values during the resolution transformation. Further investigations will be needed to address this issue. The maximum scaling effects in an averaged FVC calculation (the difference between the FVC values at the extreme resolution levels), along with the actual FVC values, are then derived. These values were also found to be a function of the endmember spectra assumed in the model and over the target area.

The mechanism underlying the scaling effects observed in FVC calculations was analyzed in terms of the function monotonicity and the error bounds. The treatment developed here provides a theoretical basis for the scaling effects, which is strength of this work. The findings of this study can contribute to development of a scale-invariant algorithm for FVC retrieval under scenarios in which multiple datasets collected at different spatial resolutions are integrated in a single analysis.

Since the analyses have been performed based on two-endmember linear mixture model, the number of endmember spectra might be the major limitations of this work. For instance, increase of the number of endmember spectra would cause differences in the monotonic behavior to some extent. This point still remains unclear from this work, which should be solely investigated in the future. In addition, further validations of the findings with actual satellite data will also be needed as future efforts.

Acknowledgments

This work was supported by The Circle for the Promotion of Science and Engineering (KO), a NASA grant NNX11AH25G (TM), and JSPS KAKENHI 21510019 (HY).

References

1. Krinner, G.; Viovy, N.; de Noblet-Ducoudré, N.; Jérôme, O.; Polcher, J.; Friedlingstein, P.; Ciais, P.; Sitch, S.; Prentice, I.C. A dynamic global vegetation model for studies of the coupled atmosphere-biosphere system. *Glob. Biogeochem. Cy.* **2005**, *19*, GB1015.
2. Myneni, R.B.; Keeling, C.D.; Tucker, C.J.; Asrar, G.; Nemani, R.R. Increased plant growth in the northern high latitudes from 1981 to 1991. *Nature* **1997**, *386*, 698–702.
3. Smith, M.O.; Ustin, S.L.; Adams, J.B.; Gillespie, A.R. Vegetation in deserts: I. A regional measure of abundance from multispectral images. *Remote Sens. Environ.* **1990**, *31*, 1–26.
4. Harrison, S.J.H.A.R. The NDVI and spectral decomposition for semi-arid vegetation abundance estimation. *Int. J. Remote Sens.* **1998**, *19*, 3109–3125.
5. Shimabukuro, Y.E.; Smith, J.A. The least-squares mixing models to generate fraction images derived from remote sensing multispectral data. *IEEE Trans. Geosci. Remote Sens.* **1991**, *29*, 16–20.
6. Xiao, J.; Moody, A. A comparison of methods for estimating fractional green vegetation cover within a desert-to-upland transition zone in central New Mexico, USA. *Remote Sens. Environ.* **2005**, *98*, 237–250.

7. Kallel, A.; Héarat-Masclé, S.L.; Ottlé, C.; Hubert-Moy, L. Determination of vegetation cover fraction by inversion of a four-parameter model based on isoline parametrization. *Remote Sens. Environ.* **2007**, *111*, 553–566.
8. Baret, F.; Hagolle, O.; Geiger, B.; Bicheron, P.; Miras, B.; Huc, M.; Berthelot, B.; Nino, F.; Weiss, M.; Samain, O.; Roujean, J.L.; Leroy, M. LAI, fAPAR and fCover CYCLOPES global products derived from VEGETATION: Part 1: Principles of the algorithm. *Remote Sens. Environ.* **2007**, *110*, 275–286.
9. Verhoef, W. Light scattering by leaf layers with application to canopy reflectance modeling: The SAIL model. *Remote Sens. Environ.* **1984**, *16*, 125–141.
10. Jacquemoud, S.; Baret, F. PROSPECT: A model of leaf optical properties spectra. *Remote Sens. Environ.* **1990**, *34*, 75–91.
11. Jiang, L.; Kogan, F.N.; Guo, W.; Tarpley, J.D.; Mitchell, Kenneth E. and Ek, M.B.; Tian, Y.; Zheng, W.; Zou, C.Z.; Ramsay, B.H. Real-time weekly global green vegetation fraction derived from advanced very high resolution radiometer-based NOAA operational global vegetation index (GVI) system. *J. Geophys. Res.* **2010**, *115*, D11114.
12. Bacour, C.; Baret, F.; Beal, D.; Weiss, M.; Pavageau, K. Neural network estimation of LAI, fAPAR, fCover and LAI×Cab, from top of canopy MERIS reflectance data: Principles and validation. *Remote Sens. Environ.* **2006**, *105*, 313–325.
13. Garcia-Haro, F.; Sommer, S.; Kemper, T. A new tool for variable endmember spectral mixture analysis. *Int. J. Remote Sens.* **2005**, *26*, 2135–2162.
14. Hansen, M.; DeFries, R.; Townshend, J.; Sohlberg, R.; Dimiceli, C.; Carroll, M. Towards an operational MODIS continuous field of percent tree cover algorithm: examples using AVHRR and MODIS data. *Remote Sens. Environ.* **2002**, *83*, 303–319.
15. Al-Hamdan, M.; Cruise, J.; Rickman, D.; Quattrochi, D. Effects of spatial and spectral resolutions on fractal dimensions in forested landscapes. *Remote Sens.* **2010**, *2*, 611–640.
16. Gallo, K.; Ji, L.; Reed, B.; Eidenshink, J.; Dwyer, J. Multi-platform comparisons of MODIS and AVHRR normalized difference vegetation index data. *Remote Sens. Environ.* **2005**, *99*, 221–231.
17. Gu, Y.; Brown, J.F.; Miura, T.; Van Leeuwen, W.J.D.; Reed, B.C. Phenological classification of the United States: A geographic framework for extending multi-sensor time-series data. *Remote Sens.* **2010**, *2*, 526–544.
18. Pouliot, D.; Latifovic, R.; Fernandes, R.; Olthof, I. Evaluation of compositing period and AVHRR and MERIS combination for improvement of spring phenology detection in deciduous forests. *Remote Sens. Environ.* **2011**, *115*, 158–166.
19. Miller, R.L.; Liu, C.C.; Buonassissi, C.J.; Wu, A.M. A multi-sensor approach to examining the distribution of Total Suspended Matter (TSM) in the Albemarle-Pamlico Estuarine System, NC, USA. *Remote Sens.* **2011**, *3*, 962–974.
20. Dal’Asta, A.P.; Brigatti, N.; Amaral, S.; Sobral Escada, M.I.; Vieira Monteiro, A.M. Identifying spatial units of human occupation in the Brazilian Amazon using Landsat and CBERS multi-resolution imagery. *Remote Sens.* **2012**, *4*, 68–87.

21. Arai, E.; Shimabukuro, Y.E.; Pereira, G.; Vijaykumar, N.L. A multi-resolution multi-temporal technique for detecting and mapping deforestation in the Brazilian Amazon rainforest. *Remote Sens.* **2011**, *3*, 1943–1956.
22. Zhang, X.; Yan, G.; Li, Q.; Li, Z.L.; Wan, H.; Guo, Z. Evaluating the fraction of vegetation cover based on NDVI spatial scale correction model. *Int. J. Remote Sens.* **2006**, *27*, 5359–5372.
23. Strahler, A.H.; Woodcock, C.E.; Smith, J. On the nature of models in remote sensing. *Remote Sens. Environ.* **1986**, *20*, 121–139.
24. Woodcock, C.E.; Strahler, A.H. The factor of scale in remote sensing. *Remote Sens. Environ.* **1987**, *21*, 311–332.
25. Marceau, D.J.; Howarth, P.J.; Gratton, D.J. Remote sensing and the measurement of geographical entities in a forested environment. 1. The scale and spatial aggregation problem. *Remote Sens. Environ.* **1994**, *49*, 93–104.
26. Marceau, D.J.; Gratton, D.J.; Fournier, R.A.; Fortin, J.P. Remote sensing and the measurement of geographical entities in a forested environment. 2. The optimal spatial resolution. *Remote Sens. Environ.* **1994**, *49*, 105–117.
27. Fisher, P. The pixel: A snare and a delusion. *Int. J. Remote Sens.* **1997**, *18*, 679–685.
28. Quattrochi, D.A.; Goodchild, M.F. *Scale in Remote Sensing and GIS*; Lewis Publishers, CRC Press: Boca Raton, FL, USA, 1997.
29. Marceau, D.J.; Hay, G.J. Remote sensing contributions to the scale issue. *Can. J. Remote Sens.* **1999**, *25*, 357–366.
30. Wu, H.; Li, Z.L. Scale issues in remote sensing: A review on analysis, processing and modeling. *Sensors* **2009**, *9*, 1768–1793.
31. Openshaw, S. *The Modifiable Areal Unit Problem*; Geo Books: Norwich, UK, 1984.
32. Townshend, J.R.G.; Justice, C.O. Selecting the spatial resolution of satellite sensors required for global monitoring of land transformations. *Int. J. Remote Sens.* **1988**, *9*, 187–236.
33. Raffy, M. Heterogeneity and change of scale in models of remote sensing. *Int. J. Remote Sens.* **1994**, *15*, 2359–2380.
34. Hu, Z.; Islam, S. A frame work for analyzing and designing scale invariant remote sensing algorithms. *IEEE Trans. Geosci. Remote Sens.* **1997**, *35*, 747–755.
35. Jiang, Z.; Huete, A.R.; Chen, J.; Chen, Y.; Yan, G.; Zhang, X. Analysis of NDVI and scaled difference vegetation index retrievals of vegetation fraction. *Remote Sens. Environ.* **2006**, *101*, 366–378.
36. Chen, J.M. Spatial scaling of a remotely sensed surface parameter by contexture. *Remote Sens. Environ.* **1999**, *69*, 30–42.
37. Garrigues, S.; Allard, D.; Baret, F.; Weiss, M. Influence of landscape spatial heterogeneity on the non-linear estimation of leaf area index from moderate spatial resolution remote sensing data. *Remote Sens. Environ.* **2006**, *105*, 286–298.
38. Sprintsin, M.; Karnieli, A.; Berliner, P.; Rotenberg, E.; Yakir, D.; Cohen, S. The effect of spatial resolution on the accuracy of leaf area index estimation for a forest planted in the desert transition zone. *Remote Sens. Environ.* **2007**, *109*, 416–428.

39. Raffy, M. Change of scale in models of remote sensing: A general method for spatialization of models. *Remote Sens. Environ.* **1992**, *40*, 101–112.
40. Yoshioka, H.; Wada, T.; Obata, K.; Miura, T. Monotonicity of Area Averaged NDVI as a Function of Spatial Resolution Based on a Variable Endmember Linear Mixture Model. In *Proceedings of IEEE IGARSS08*, Boston, MA, USA, 6–11 July 2008; Volume III, pp. 415–418.
41. Obata, K.; Wada, T.; Miura, T.; Yoshioka, H. Scaling effect of area-averaged NDVI: Monotonicity along the spatial resolution. *Remote Sens.* **2012**, *4*, 160–179.
42. Zeng, X.; Dickinson, R.E.; Walker, A.; Shaikh, M.; Defries, R.S.; Qi, J. Derivation and evaluation of global 1-km fractional vegetation cover data for land modeling. *J. Appl. Meteorol.* **2000**, *39*, 826–839.
43. Hirano, Y.; Yasuoka, Y.; Ichinose, T. Urban climate simulation by incorporating satellite-derived vegetation cover distribution into a mesoscale meteorological models. *Theor. Appl. Climatol.* **2004**, *79*, 175–184.
44. Obata, K.; Miura, M.; Yoshioka, H. Scaling effect of fraction of vegetation cover retrieved by algorithms based on linear mixutre model. *Proc. SPIE* **2010**, *7809*, 78095.
45. Obata, K.; Yoshioka, H. Inter-algorithm relationships for the estimation of the fraction of vegetation cover based on a two endmember linear mixture model with the VI constraint. *Remote Sens.* **2010**, *2*, 1680–1701.
46. Song, C. Spectral mixture analysis for subpixel vegetation fractions in the urban environment: How to incorporate endmember variability? *Remote Sens. Environ.* **2005**, *95*, 248–263.
47. Bateson, C.A.; Asner, G.P.; Wessman, C.A. Endmember bundles: a new approach to incorporating endmember variability into spectral mixture analysis. *IEEE Trans. Geosci. Remote Sens.* **2000**, *38*, 1083–1094.
48. Settle, J. On the effect of variable endmember spectra in the linear mixture model. *IEEE Trans. Geosci. Remote Sens.* **2006**, *44*, 389–396.
49. Raffy, M. The role of spatial resolution in quantification problems: Spatialization method. *Int. J. Remote Sens.* **1994**, *15*, 2381–2392.
50. Gregoire H.C.; Raffy, M. Elaboration of multispectral models for heterogeneous media: Application to the LAI. *Remote Sens. Rev.* **1997**, *15*, 223–234.
51. Raffy, M.; Gregoire, C. Semi-empirical models and scaling: A least square method for remote sensing experiments. *Int. J. Remote Sens.* **1998**, *19*, 2527–2541.